ADVANCED ELECTRONIC MATERIALS
www.advelectronicmat.de

Tungsten-Disulfide/Polyaniline High Frequency Supercapacitors

*Amrita De Adhikari, Nitzan Shauloff, Yury Turkulets, Ilan Shalish, and Raz Jelinek**

Transition metal dichalcogenides are considered promising constituents in energy storage devices due to their large surface areas, 2D sheet structures, and occurrence of efficient redox reactions at their surfaces. Supercapacitors comprising WS_2-polyaniline (PANI) composite electrodes which exhibit excellent electrochemical properties, particularly effective high frequency response, are constructed. The highly porous WS_2-PANI device facilitate rapid ion transport and surface access, aiding rapid reversible redox reactions contributing to the high frequency pseudocapacitive profile of the device. The symmetric WS_2-PANI supercapacitor displays significantly higher capacitance of 180 μF cm^{-2} at a frequency of 120 Hz. This study points to potential application of WS_2 composites in high frequency applications such as alternating current line filtering, and may open new avenues for employing the material in energy storage applications.

1. Introduction

Attaining high-frequency response is considered central to supercapacitor design and applications. This objective is particularly important in applications such as high-energy pulses and alternating current (AC) line-filtering, in which AC signals are transformed into stable direct current (DC) output.[1–3] While aluminum electrolytic capacitors (AECs) exhibit good capacitive behavior at high frequencies, they display low volumetric capacitance and thus have limited applicability in electronic devices due to the required capacitor size. Supercapacitors (SCs), which exhibit orders-of-magnitude higher volumetric capacitance than AECs, may substitute traditional capacitors. Yet, SCs display rapid decrease in capacitive behavior in high frequencies.[4–6] The pioneering study by Miller et al. demonstrated a SCs comprising vertically oriented graphene sheets that featured good AC line filtering at 120 Hz with a resistance–capacitance (RC) time constant of 200 μs.[1] Other reports in recent years have demonstrated electric double layer capacitance (EDLC)-based SCs consisting of carbon nanotube carpets,[2] coordination polymer framework,[3] printable graphene,[4] vertically-oriented carbon nanowall foam,[5] and others. Practical applicability of EDLC-based high frequency SCs has been restricted, however, because of their complex and expensive synthetic procedures.[6] Further, the low material densities of EDLC materials require high mass loadings to attain high capacitance.[2,4]

Pseudocapacitive-based SCs generally exhibit higher specific capacitance and energy density compared to EDLCs, therefore much thinner layers of pseudocapacitive materials are required for effective applications.[7,8] Pseudocapacitive-based SCs have been considered as having inferior potential in high frequency applications due to the presumed slow kinetics of interfacial redox reactions[9]; recent studies, however, have shown that redox kinetics do not, in fact, constitute a barrier for high frequency capacitance applications.[10] Among the strategies for improving frequency response of pseudocapacitive SCs has been lowering the electrolytic resistance in 2D materials. Specifically, the combination of high surface area nanosheets and high interlayer distance provide multiple sites for ion exchange, thereby accelerating ion diffusion accounting for high specific capacitance and energy density.[11,12] Various 2D materials including transition metal carbides (Mxenes)[14,15] and transition metal dichalcogenides (TMDs)[16] have been employed as SC electrodes. Recent studies reported on MXenes-based electrodes, have maintained high capacitance up to a scan rate of 1000 V s^{-1}.[15] However, the low stability of MXenes in high voltage limits practical applicability of such devices.[17,18]

2D TMDs have attracted particular interest as supercapacitor platforms due to their favorable electrochemical properties, large specific surface area, reversible redox reactions at the transition metal centers, and interlayer spacing accommodating ionic species.[19–21] Specifically, MoS_2, WS_2, or VS_2 have been employed in varied energy storage devices.[22–25] 2D TMDs materials have been also considered as candidates for high frequency applications. Sellam et al., for example, reported SCs based on $MoS_{2x}Se_{2(1-x)}$ for AC line filtering.[29] Notably, the X-M-X layers exhibit weak van der Waals forces with the intercalated metal ions, facilitating fast reversible redox reaction.[26,27] However, TMDs generally exhibit poor capacitance

Dr. A. De Adhikari, N. Shauloff, Prof. R. Jelinek
Department of Chemistry
Ben-Gurion University of the Negev
Beer Sheva 8410501, Israel
E-mail: razj@bgu.ac.il
Y. Turkulets, Prof. I. Shalish
School of Electrical Engineering
Ben-Gurion University
Beer Sheva 8410501, Israel
Prof. R. Jelinek
Ilse Katz Institute for Nanotechnology
Ben-Gurion University of the Negev
Beer Sheva 8410501, Israel

DOI: 10.1002/aelm.202100025

retention[30] and complex multilayer hybrid architectures have been introduced to overcome this limitation.[31]

Here we demonstrate for the first time a WS_2-based high frequency SCs exhibiting excellent electrochemical properties. Specifically, WS_2-PANI based electrodes were prepared via simple electrochemical deposition on a commercially available nickel foil current collector. PANI is a widely-used conducting polymer[32–34] and the composite WS_2-PANI electrodes created a highly microporous morphology furnishing extensive surface area and facilitating efficient ion diffusion. A symmetric SC comprising the WS_2-PANI electrodes displayed excellent capacitive behavior at high frequencies, featuring a very small RC time constant of 151 µs and a phase angle of –75.9° at 120 Hz. The WS_2-PANI symmetric SC device featured capacitive response even at high scan rates (up to 5000 V s^{-1}), high specific capacitance of 72.27 F g^{-1} at a current density of 1 A g^{-1}.

2. Results and Discussion

2.1. Synthesis and Characterization of WS_2-PANI Electrodes

Figure 1 depicts the simple synthesis scheme of the WS_2-PANI electrode. We utilized commercially available WS_2 sheets, which were dispersed in H_2SO_4/ACN and exfoliated by sonication. Following addition of aniline monomers, the solution was electrodeposited on a flexible nickel foil serving as the current collector, yielding a thin layer comprising crosslinked PANI nanofibers embedding the WS_2 nanosheets electrode.[35] Notably, the WS_2-PANI electrode was flexible, withstood repeated bending (Figure S1, Supporting Information), was stable for long time periods, and did not undergo degradation in operating conditions.

The WS_2-PANI electrodes were characterized microscopically and spectroscopically (**Figure 2**). Figure 2A depicts a representative scanning electron microscopy (SEM) image of a WS_2-PANI electrode. The SEM image shows the microporous PANI framework embedding sheet-like WS_2 flakes (whitish flakes in image, confirmed by elemental mapping Figure S2, Supporting Information). Notably, inclusion of WS_2 within the PANI layer did not adversely affect the overall porosity of the polymer (Figure S2, Supporting Information).[36] This feature is important, as a microporous electrode organization is important for efficient ion diffusion which is essential for SCs performance.[37] AFM analysis (Figure S3, Supporting Information) indicates thickness range of 3–4 nm of the WS_2 domains, corresponding to 2–6 exfoliated layers.[38]

Brunauer–Emmett–Teller (BET) analysis in Figure 2B complements the SEM experiment, attesting to the high porosity and extensive internal surface area of the WS_2-PANI electrodes. The WS_2-PANI electrodes displayed a type IV isotherm with hysteresis (Figure 2B, blue curve), indicating porous, high surface area architecture.[39] Notably, electrodes comprising only PANI (black curve in Figure 2B) or WS_2 (red curve) exhibited lower surface area and less porous organization.[40] The specific surface area of the WS_2-PANI electrode, calculated from the BET data, at around 70 m^2 g^{-1} was significantly higher than the pure PANI or WS_2 electrodes (TableS1, Supporting Information). Importantly, this value is greater than corresponding surface areas in previously reported WS_2-carbon composite,[41] WS_2/g-C_3N_4,[42] 1T-WS_2@TiO_2@Ti_3C_2.[43]

The X-ray diffraction (XRD) analysis in Figure 2C illuminates the crystalline properties of the WS_2-PANI electrode and structural modulations in comparison with films comprising pure PANI or pure WS_2. Specifically, most XRD peaks corresponding to the individual PANI (black pattern in Figure 2C) and WS_2 (red) constituents appear in the XRD pattern of the composite WS_2-PANI film (blue pattern), although distinct shifts and peak broadenings are apparent. Note, in particular, the significant attenuation of the WS_2 signal at around 13° corresponding to (002) planes which is close to the (011) plane of PANI, indicates that there is exfoliation along the (002) plane due to the incorporation of the PANI fibers.[44]Furthermore, the shift and broadening of the PANI peak at 40° account for increased inter-chain separation of the PANI backbone due to the presence of WS_2 sheets within the PANI network.[45]

The micro Raman spectroscopy data in Figure 2D further underscores the interactions between PANI and WS_2 in the composite electrode. In particular, the Raman spectrum of WS_2-PANI film (blue spectrum, Figure 2D) reveals distinct shifts and broadening of the peaks at 355 and 420 cm^{-1} in the WS_2 Raman scattering result (red spectrum, Figure 2D) ascribed to the E^1_{2g} (in-plane optical mode) and A_{1g} (out-of plane vibration mode) modes, respectively.[46] These peak transformations likely account for the dispersion of the WS_2 sheets within the PANI network via interactions of with nitrenium cations of aniline.[47,48] Furthermore, the significant changes in the spectral positions and widths of the Raman signals around 600 cm^{-1} between pure PANI (black spectrum) and WS_2-PANI (blue spectrum) indicate conformational changes induced by incorporation of the WS_2 domains within the PANI matrix, resulting in more planar chains.[49] X ray photoelectron spectroscopy (XPS) data (Figure S4, Supporting Information) confirm embedding of WS_2 nanosheets within the PANI matrix.[50,51]

Figure 1. Fabrication of the WS_2-polyaniline electrode. Co-dispersion of exfoliated WS_2 and aniline monomers followed by electrodeposition on thin nickel foil.

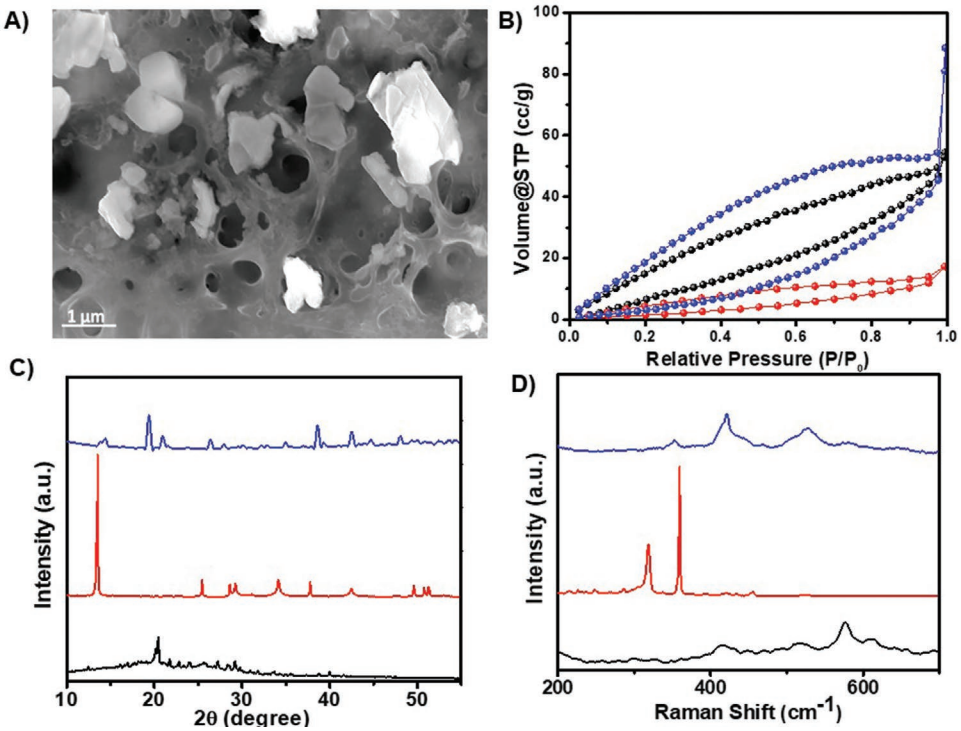

Figure 2. Microscopic and spectroscopic characterization. A) SEM image of the WS_2-PANI electrode. B) Brunauer–Emmett–Teller (BET) analysis. WS_2 layer (red curve), PANI (black), and WS_2-PANI (blue). C) XRD patterns of pure electrodeposited PANI film (black), WS_2 (red) and WS_2-PANI (blue). D) Raman scattering spectra of PANI (black), WS_2 (red), and WS_2-PANI (blue).

2.2. Electrochemical Properties of a Symmetric WS_2-PANI Supercapacitor

We fabricated a symmetric WS_2-PANI supercapacitor by using two WS_2-PANI electrodes with polystyrene (PS) film as a spacer and 1 **M** Na_2SO_4 as the electrolyte (the device is illustrated in Figure S5, Supporting Information) and investigated its electrochemical properties and frequency response (**Figures 3–5**). Figure 3 depicts the cyclic voltammograms (CV) recorded at different scan rates (100–5000 V s^{-1}) at a potential window of 0–0.8 V. The CV curves display quasi-rectangular shapes reflecting good capacitive behavior of the WS_2-PANI SCs.[52] The favorable capacitive profile likely corresponds to efficient ion intercalation and complementarity between the oxidation states of PANI and valence states of tungsten active sites.[53–56] A linear dependence between discharge current and scan rate as in Figure 3D, up to 5000 V s^{-1}, underscores an effective capacitive response, reflecting efficient ion diffusion and interfacial faradaic reactions.[55,57,58] The areal capacitance of 331 μF cm^{-2} at 5000 V s^{-1} (Figure S6, Supporting Information) is superior compared to varied high power SCs.[29] The theoretical capacitance, calculated through Trasatti method, was 6 mF cm^{-2}.

The pseudocapacitance mechanism of the new WS_2-PANI device was aided by the solvent exfoliation method. Specifically, the PANI network entraps the WS_2 domains effectively linking the WS_2 sheets.[59] In particular, during the polymerization process, the protonated aniline monomers initially transformed into aniline nitrenium cations and nucleation sites were likely generated on the surface of WS_2.[60] The electroactive materials store charge via two possible mechanisms. Specifically, alkali metal cation (Na^+) from the electrolyte (Na_2SO_4) diffuses and intercalates within the WS_2 layers, according to the following reaction:[61,62]

$$WS_2 + Na^+ + e^- \rightarrow WS - SNa \quad (1)$$

An alternative pathway involves adsorption of the sodium ions at the electrode/electrolyte interface, according to following Scheme:

$$WS_2 + Na^+ + e^- \rightarrow WS_2 - Na \quad (2)$$

Indeed, intercalation/release of the relatively large sodium ions further allows exfoliation of the WS_2 layers leading to an increased surface area and consequently higher specific capacitance.[23] Moreover, using Trasatti's method, the percentage contribution from pseudocapacitance and ELDC was calculated, confirming that the system is more dominated by pseudocapacitive contribution which occurs owing to the synergistic effect between the PANI and WS_2 sheets leading to high overall capacitance.[63]

Electrochemical impedance spectroscopy (EIS) was applied to examine the frequency response of the WS_2-PANI SCs, in comparison to symmetric SCs fabricated from pure PANI or pure WS_2 electrodes (Figure 4). The Nyquist plots in Figure 4A do not display semi-circular appearance, indicating negligible charge transfer resistance and allowing modeling of a simple circuit composed of a resistor and a capacitor connected in

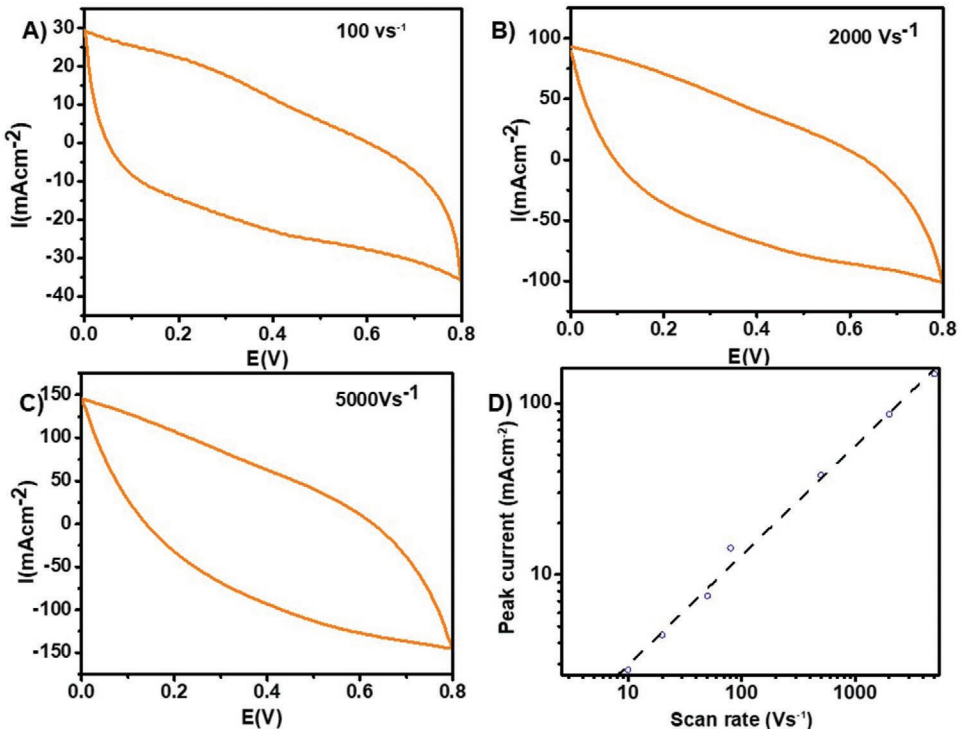

Figure 3. Cyclic voltammogram (CV) of symmetric supercapacitors prepared with WS_2-PANI electrodes. A–C). CV curves recorded at the indicated different scan rates. D) Discharge peak current as a function of the scan rate recorded for SCs constructed using the WS_2-PANI electrodes. Both scales are logarithmic. A linear fit is plotted (broken line).

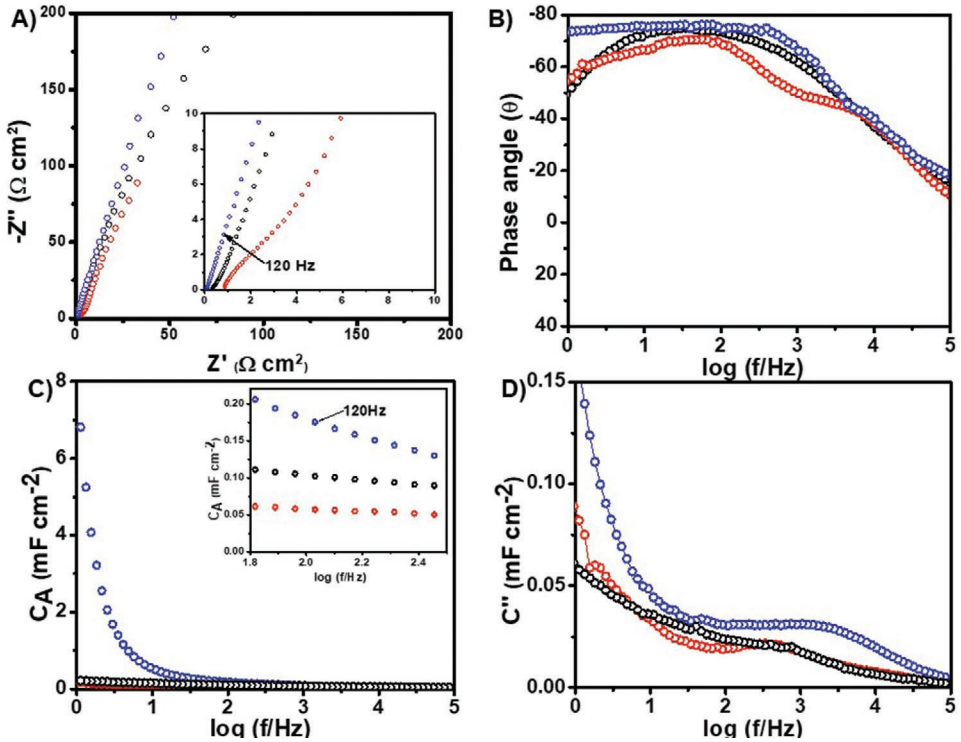

Figure 4. Electrochemical impedance spectroscopy of symmetric WS_2/PANI supercapacitors. Data recorded for symmetric SCs comprising WS_2-PANI electrodes (blue curves), pure PANI (black curves) electrodes, and pure WS_2 (red curves) electrodes. A) Nyquist plot (inset showing the high frequency region). B) Phase angle as a function of log (*f*/Hz) (Bode plot). C) Areal capacitance as a function of log (*f*/Hz) (inset showing the magnified view at 120 Hz. D) Imaginary component of the capacitance as a function of log (*f*/Hz).

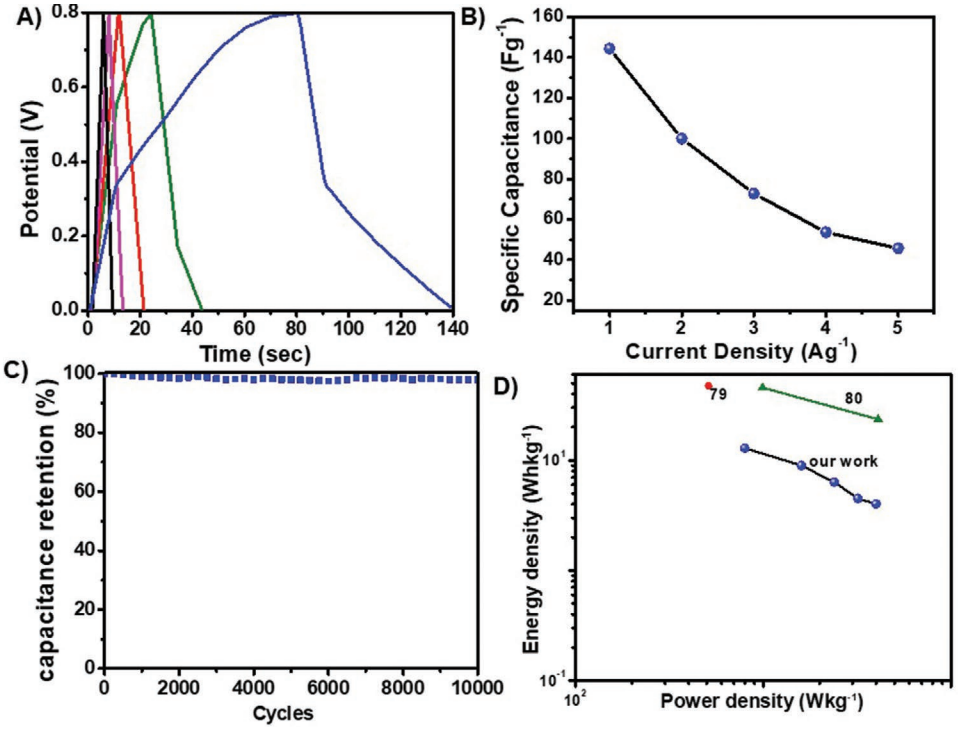

Figure 5. Capacitance properties of the symmetric WS_2-PANI supercapacitor. A) Galvanostatic charge discharge curves at various current densities. 1 A g^{-1} (blue), 2 A g^{-1} (green), 3 A g^{-1} (red), 4 A g^{-1} (pink), 5 A g^{-1} (black). B) Specific capacitance as a function of current density. C) Percentage capacitance retention at a current density of 10 A g^{-1}. D) Ragone plot depicting the variation of energy density with power density (both scales are logarithmic).

series.[1,2] The lower initial resistance (i.e., real impedance component) of WS_2-PANI SCs (Figure 4A, blue curve) compared to either pure PANI (black curve) or pure WS_2 (red curve) SCs is ascribed to the pronounced porous morphology and higher surface area of the composite WS_2-PANI electrodes (Figure 2A,B). Similarly, the resistance at 120 Hz, calculated from the real part of the impedance (magnified plot of the high frequency region, inset in Figure 4A), yielded 0.84, 1.5, and 5.8 Ω cm^2 for the WS_2-PANI SC, PANI SC, and WS_2 SC, respectively. The lower resistance of the WS_2-PANI SC at 120 Hz accounts for the microporous architecture of the composite electrodes resulting in reduced geometrical resistance.[64,65] Importantly, the RC time constant at 120 Hz of the WS_2-PANI SC—151 µs—is far smaller than either commercially available AECs[66] or high frequency TMD SCs.[29,55] Figure S7, Supporting Information presents EIS data indicating optimization of the deposition time of the electroactive material.

To assess the frequency-dependent capacitor behavior of the devices, the phase angles as a function of log (f/Hz) were calculated (e.g., Bode plot, Figure 4B). The Bode plot in Figure 4B indicates phase angles of –75.9°, –71.6° and –68.5° at 120 Hz, for the WS_2-PANI, PANI, and WS_2 SCs devices, respectively. The phase angle calculated for the WS_2-PANI SC reflects an excellent capacitor behavior at the AC line filtering working frequency of 120 Hz. In particular, the phase angle recorded for WS_2-PANI is close to –83.9° phase angle in commercial AECs,[66] and better than previously reported TMD-based high frequency SCs. The frequency at –45° for the WS_2-PANI SC, accounting for an equal capacitor and resistor behavior, was ≈6 kHz, better than previously-reported high frequency SCs like, meso/macroporous carbon sponge[67], plasma pyrolyzed bacterial cellulose aerogel[68] underscoring the feasibility for operation of the WS_2-PANI SC at frequencies exceeding 1 kHz.

Figure 4C presents the specific areal capacitance (C_A) of the fabricated SCs as a function of frequency. The C_A in case of WS_2-PANI (blue curve) is exceptionally high compared to others (PANI and WS_2), thus suggesting a small resistive loss. In particular, the decrease in the capacitance of the WS_2-PANI SC between 1 and 120 Hz is more moderate than previously reported SCs, in which diffusion of ions become more restricted at lower frequencies.[13,69] Notably, in 120 Hz (Figure 4C, inset) the WS_2-PANI SC exhibits significantly higher capacitance (180 µF cm^{-2}, blue data points) compared to the PANI device (105 µF cm^{-2}, black) or pure WS_2 (50 µF cm^{-2}, red).

Figure 4D presents the relaxation time (τ_0; the minimum time for discharging the energy from the device with at least 50% efficiency)[70] of the WS_2-PANI SC calculated from the maximum in the imaginary capacitance graph.[2,70] The calculated τ_0 of 0.54 ms underscores the potential application of the device in high frequency applications. Indeed, such a low value, particularly compared to corresponding relaxation times in state-of-the-art EDLC-based SCs,[2,4,71] indicates that the primary kinetic barriers in high frequency SC applications in the case of the WS_2-PANI electrode are likely related to ion diffusion rather than the actual redox reactions.[14,72] Overall, the EIS data in Figure 4 attest to the ultrahigh frequency performance

of the WS_2-PANI SC, pointing to feasibility of AC line-filtering applications.[73]

Figure 5 depicts the electrochemical profile of the WS_2-PANI SC. The galvanostatic charge discharge (GCD) curves of the device at different current densities (1–5 A g^{-1}) within a potential range 0–0.8 V (Figure 5A) illuminate the charge storage properties of the electrodes. The asymmetric shapes of the GCD curves in Figure 5A reflect the pseudocapacitive behavior of the electrode material.[74,75] The specific capacitance calculated from the GCD curves is presented in Figure 5B. Capacitance of 72.3 F g^{-1} was obtained at 1 A g^{-1} current density for the WS_2-PANI device corresponding to 289 F g^{-1} for a single electrode when multiplying by four, the coefficient employed according to the method depicted by Ruoff et al.[76] Figure 5B further shows a gradual decrease in specific capacitance in higher current densities, ascribed to the slow redox reactions at the electrode interface; similar drop in specific capacitance has been previously reported.[77,78]

Figure 5C underscores the excellent electrochemical stability of the WS_2-PANI device, an important feature in potential energy storage applications. Specifically, the WS_2-PANI device exhibits capacitance retention of 98% up to 10 000 cycles. Figure 5D further demonstrates the excellent energy and power storage capabilities of the WS_2-PANI device, attaining high energy density of 6.42 Wh kg^{-1} in power density of 399.9 W kg^{-1} and energy density of 2.03 Wh kg^{-1} at a power density of 1996.7 W kg^{-1} as compared with previous reports.[79,80]

Figure 6 highlights the excellent AC line filtering capability of the WS_2-PANI supercapacitor. The scheme in Figure 6A illustrates the AC-to-DC converter circuit. In the experiment, a 5 V peak-to-peak sinusoidal signal at 120 Hz was used as input through a full-wave bridge rectifier. Rectification was followed by filtering using the WS_2-PANI supercapacitor, resulting in a substantially smoothed output signal (Figure S8, Supporting Information). As shown in Figure 6B, the filtering performance of the WS_2-PANI device was comparable to a commercial 1000 µF AEC, as both yielded highly effective DC. However, the WS_2-PANI supercapacitor is orders of magnitude smaller in volume and weight compared to the AEC, underscoring its potential as an attractive substitute.

The electrochemical data presented in Figures 3–6 attest to the attractive properties and practical potential of the WS_2-PANI device. WS_2 has emerged as a smart electrode material for SCs because of its intrinsically layered structure and high capacitance. Tungsten also exhibits a wide range of oxidation states, making it a promising pseudocapacitive material. WS_2, however, often displays interlayer stacking leading to poor conductivity and capacitance fading. Accordingly, integration of the WS_2 with the PANI fibers results in more pronounced WS_2 interlayer distance, greater surface area, and faster diffusion of the electrolyte ions.

Different than EDLC-based materials (particularly graphene or carbon nanotubes) that have been explored as substrates for high frequency SCs, WS_2 is intrinsically 2D thereby contributing to excellent pseudocapacitive properties facilitating fast, reversible surface Faradaic reactions. WS_2-based SCs further exhibit high specific capacitance and low ESR.[81] Particularly in the case of the new WS_2-PANI system presented here, the

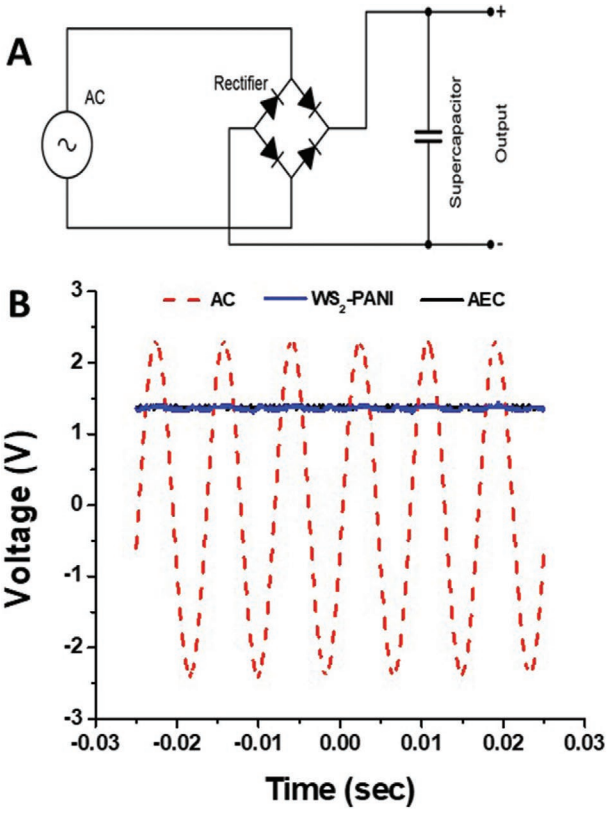

Figure 6. AC-line filtering by the WS_2-PANI supercapacitor. A) Schematic diagram of the AC-to-DC converter. B) Input AC wave (red dashed line) and the resulting DC signal obtained after filtering using the WS_2-PANI supercapacitor (blue line) and a commercial 1000 µF aluminum electrolytic capacitor (AEC; black line).

electrodes were synthesized by direct growth of the electroactive material on the conductive substrate (inexpensive and commercially available nickel foil) via electrochemical method. As such, external polymer binders (which would increase the series resistance) were not required.

3. Conclusions

This work demonstrates fabrication, for the first time, of high frequency supercapacitor based upon WS_2. Specifically, a symmetrical device comprising porous WS_2-PANI device exhibited excellent electrochemical properties, including high capacitance of 72.27 F g^{-1} at 1 A g^{-1} (331 mF cm^{-2} at 5000 V s^{-1}) and considerable high energy density of 6.42 Wh kg^{-1} at power density of 399.9 W kg^{-1}.In particular, the WS_2-PANI device displayed an exceptional high frequency response of ≈6 kHz with a high areal capacitance of 180 µF cm^{-2} and a bode phase angle of –75.9° at 120 Hz. The attractive electrochemical performance we report is likely among one of the efficient high frequency SCs compared to previously reported TMDs high frequency SCs. Importantly, the electrode synthesis procedure was simple, utilizing inexpensive and readily available reagents, making the system amenable for upscaling and practical applicability. Overall, the pronounced charge storage with very

low resistance, capacitance retention (up to 10 000 cycles), and high frequency capacitance attained make WS_2-PANI a promising material for advanced energy storage applications, particularly a viable alternative for commercially-available AECs.

4. Experimental Section

Materials: Ni foil, 30 µm thick, was purchased from MTI Corporation. WS_2 powder, 2 µm (99%), aniline monomer, and Polystyrene (PS) ($M_w \approx$ 280 kDa) were purchased from Sigma Aldrich. Dimethylformamide (DMF) was purchased from J. T. Baker, and Na_2SO_4 (anhydrous 99%) was purchased from Loba Chemie. All chemicals were used as received. The water used in the experiments were doubly purified by a Barnstead D7382 water purification system (Barnstead Thermolyne, Dubuque, IA), at 18.2 MΩ cm resistivity.

Electrode Fabrication: Electrodes were fabricated by electrochemical deposition employing a three-electrode configuration with Ni foil as the working electrode, Pt as the counter electrode and Ag/AgCl as the reference electrode. Initially, WS_2 was dispersed homogenously via ultrasonication in 0.1 M H_2SO_4/ACN electrolytic solution. To this solution 0.05 M aniline monomers were added and electrodeposition was carried out by cyclic voltammetry between 0 and 1.2 V versus the reference electrode at a scan rate of 10 V s^{-1} for 2, 4, 6, and 8 min consecutively in order to identify the optimal deposition time of 4 min. The electrodes obtained after electrodeposition were washed and dried prior to performing the experiments.

Spacer Fabrication: A homogenous PS solution was prepared in DMF (30% w/v). Using this homogenous solution, PS fibers were electrospun on a glass slide for 40 min (under a 20 kV voltage and 22 cm between needle and collector) and then annealed at 100 °C for 15 min. The film was then rinsed with water three times. Finally, the film was preserved in 1 M Na_2SO_4 solution to avoid drying.

Device Fabrication: Symmetric SCs were composed of two WS_2-PANI electrodes using the PS film spacer dipped in 1 M Na_2SO_4 solution. The devices were then tightly enveloped using a scotch tape.

AC Line Filtering: AC-to-DC converter was implemented using four 1N4148 diodes, connected in a full-wave bridge rectifier configuration, with a filtering capacitor connected parallel to the output. As a control, the same experiment was carried out using a standard 1000 µF/25 V electrolytic capacitor. The input AC signal was generated using a function waveform generator (Agilent 33220A), and the resulting output signals were measured using an oscilloscope (Agilent DSO-X 2002A) (Figure S8, Supporting Information).

Characterization: SEM images of the samples were carried out on a JEOL SEM (Tokyo, Japan, JSM-7400F). BET surface area analysis was carried out on a NOVAtouch BET instrument (Boynton beach, Florida). Powder XRD was carried out on a Panalytical Empyrean powder diffractometer (PANalytical, Almelo, Netherlands), with X-ray source of Philips ceramic sealed tube (1.8kW), at a wavelength Cu K_α (1.5405 Å). Raman scattering analysis was carried out on a LabRam HR Evolution Horiba Raman (Kyoto, Japan) using a 532 nm.

Electrochemical Measurements: Cyclic voltammetry was conducted at voltage ranges between 0 and –0.8 V. GCD measurements were conducted at current density in the range of 1–5 A g^{-1} in a voltage window of 0.8 V. Electrochemical impedance measurements were conducted between 1 Hz and 100 kHz with sinus amplitude of 5 mV. All electrochemical measurements were conducted in a 2-electrode configuration on either a CH instrument 760C (Austin, TX) or a Bio-Logic SP-150 (Claix, France).

Supporting Information

Supporting Information is available from the Wiley Online Library or from the author.

Conflict of Interest

The authors declare no conflict of interest.

Data Availability Statement

Research data are not shared.

Keywords

AC line filtering, high frequency response, polyaniline, tungsten disulfide

Received: January 8, 2021
Revised: April 15, 2021
Published online:

[1] J. R. Miller, R. A. Outlaw, B. C. Holloway, *Science* **2010**, *329*, 1637.
[2] J. Lin, C. Zhang, Z. Yan, Y. Zhu, Z. Peng, R. H. Hauge, D. Natelson, J. M. Tour, *Nano Lett.* **2013**, *13*, 72.
[3] C. Yang, K. S. Schellhammer, F. Ortmann, S. Sun, R. Dong, M. Karakus, Z. Mics, M. Löffler, F. Zhang, X. Zhuang, E. Cánovas, G. Cuniberti, M. Bonn, X. Feng, *Angew. Chem., Int. Ed.* **2017**, *56*, 3920.
[4] Z.-S. Wu, Z. Liu, K. Parvez, X. Feng, K. Müllen, *Adv. Mater.* **2015**, *27*, 3669.
[5] Z. Bo, C. Xu, H. Yang, H. Shi, J. Yan, K. Cen, K. Ostrikov, *ChemElectroChem* **2019**, *6*, 2167.
[6] P. Yang, W. Mai, *Nano Energy* **2014**, *8*, 274.
[7] B. E. Conway, *Electrochemical Supercapacitors: Scientific Fundamentals and Technological Applications*, Springer Science & Business Media, Berlin **2013**.
[8] W. Deng, X. Ji, Q. Chen, C. E. Banks, *RSC Adv.* **2011**, *1*, 1171.
[9] B. E. Conway, *J. Electrochem. Soc.* **1991**, *138*, 1539.
[10] A. Morag, N. Shauloff, N. Maman, N. Froumin, V. Ezersky, R. Jelinek, *Batteries Supercaps* **2020**, *3*, 946.
[11] E. Pomerantseva, Y. Gogotsi, *Nat. Energy* **2017**, *2*, 17089.
[12] P. Pazhamalai, K. Krishnamoorthy, S. Manoharan, S. J. Kim, *J. Alloys Compd.* **2019**, *771*, 803.
[13] D. Zhao, W. Chang, C. Lu, C. Yang, K. Jiang, X. Chang, H. Lin, F. Zhang, S. Han, Z. Hou, X. Zhuang, *Small* **2019**, *15*, 1901494.
[14] Q. Jiang, N. Kurra, K. Maleski, Y. Lei, H. Liang, Y. Zhang, Y. Gogotsi, H. N. Alshareef, *Adv. Energy Mater.* **2019**, *9*, 1901061.
[15] G. S. Gund, J. H. Park, R. Harpalsinh, M. Kota, J. H. Shin, T.-i. Kim, Y. Gogotsi, H. S. Park, *Joule* **2019**, *3*, 164.
[16] Q. Yun, L. Li, Z. Hu, Q. Lu, B. Chen, H. Zhang, *Adv. Mater.* **2020**, *32*, 1903826.
[17] C. J. Zhang, S. Pinilla, N. McEvoy, C. P. Cullen, B. Anasori, E. Long, S.-H. Park, A. Seral-Ascaso, A. Shmeliov, D. Krishnan, C. Morant, X. Liu, G. S. Duesberg, Y. Gogotsi, V. Nicolosi, *Chem. Mater.* **2017**, *29*, 4848.
[18] T. Habib, X. Zhao, S. A. Shah, Y. Chen, W. Sun, H. An, J. L. Lutkenhaus, M. Radovic, M. J. Green, *npj 2D Mater. Appl.* **2019**, *3*, 8.
[19] H. Wang, H. Feng, J. Li, *Small* **2014**, *10*, 2165.
[20] M. Chhowalla, H. S. Shin, G. Eda, L.-J. Li, K. P. Loh, H. Zhang, *Nat. Chem.* **2013**, *5*, 263.
[21] X. Chia, A. Y. S. Eng, A. Ambrosi, S. M. Tan, M. Pumera, *Chem. Rev.* **2015**, *115*, 11941.
[22] S. Ratha, C. S. Rout, *ACS Appl. Mater. Interfaces* **2013**, 11427.
[23] M. Acerce, D. Voiry, M. Chhowalla, *Nat. Nanotechnol.* **2015**, *10*, 313.

[24] C. C. Mayorga-Martinez, A. Ambrosi, A. Y. S. Eng, Z. Sofer, M. Pumera, *Electrochem. Commun.* **2015**, *56*, 24.
[25] K. Gopalakrishnan, S. Sultan, A. Govindaraj, C. N. R. Rao, *Nano Energy* **2015**, *12*, 52.
[26] T. Stephenson, Z. Li, B. Olsen, D. Mitlin, *Energy Environ. Sci.* **2014**, *7*, 209.
[27] B. Mendoza-Sánchez, Y. Gogotsi, *Adv. Mater.* **2016**, *28*, 6104.
[28] Y. Zhu, L. Peng, Z. Fang, C. Yan, X. Zhang, G. Yu, *Adv. Mater.* **2018**, *30*, 1706347.
[29] A. Sellam, R. N. Jenjeti, S. Sampath, *J. Phys. Chem. C* **2018**, *122*, 14186.
[30] M. Pumera, Z. Sofer, A. Ambrosi, *J. Mater. Chem. A* **2014**, *2*, 8981.
[31] J. Come, J. M. Black, M. R. Lukatskaya, M. Naguib, M. Beidaghi, A. J. Rondinone, S. V. Kalinin, D. J. Wesolowski, Y. Gogotsi, N. Balke, *Nano Energy* **2015**, *17*, 27.
[32] C. Yang, Z. Chen, I. Shakir, Y. Xu, H. Lu, *Nano Res.* **2016**, *9*, 951.
[33] J. Zhu, W. Sun, D. Yang, Y. Zhang, H. H. Hoon, H. Zhang, Q. Yan, *Small* **2015**, *11*, 4123.
[34] K. Wang, H. Wu, Y. Meng, Z. Wei, *Small* **2014**, *10*, 14.
[35] X. Zhang, H. S. Kolla, X. Wang, K. Raja, S. Manohar, *Adv. Funct. Mater.* **2006**, *16*, 1145.
[36] Z. Tian, H. Yu, L. Wang, M. Saleem, F. Ren, P. Ren, Y. Chen, R. Sun, Y. Sun, L. Huang, *RSC Adv.* **2014**, *4*, 28195.
[37] Y. R. Lee, I. Y. Kim, T. W. Kim, J. M. Lee, S.-J. Hwang, *Chem. - Eur. J.* **2012**, *18*, 2263.
[38] B. Adilbekova, Y. Lin, E. Yengel, H. Faber, G. Harrison, Y. Firdaus, A. El-Labban, D. H. Anjum, V. Tung, T. D. Anthopoulos, *J. Mater. Chem. C* **2020**, *8*, 5259.
[39] Z. A. Alothman, *Materials* **2012**, *5*, 2874.
[40] L. Zu, X. Cui, Y. Jiang, Z. Hu, H. Lian, Y. Liu, Y. Jin, Y. Li, X. Wang, *Materials* **2015**, *8*, 1369.
[41] S. H. Choi, S. J. Boo, J. H. Lee, Y. C. Kang, *Sci. Rep.* **2014**, *4*, 5755.
[42] P. Zeng, X. Ji, Z. Su, S. Zhang, *RSC Adv.* **2018**, *8*, 20557.
[43] Y. Li, L. Ding, S.Yin, Z. Liang, Y. Xue, X. Wang, H. Cui, J. Tian, *Nano-Micro Lett.* **2020**, *12*, 6.
[44] D. Zheng, Y.-P. Wu, Z. Y. Li, Z. B. Cai, *RSC Adv.* **2017**, *7*, 14060.
[45] J. P. Pouget, C. H. Hsu, A. G. M. Diarmid, A. J. Epstein, *Synth. Met.* **1995**, *69*, 119.
[46] R. K. Jha, M. Wan, C. Jacob, P. K. Guha, *New J. Chem.* **2018**, *42*, 735.
[47] C. Rice, R. J. Young, R. Zan, U. Bangert, D. Wolverson, T. Georgiou, R. Jalil, K. S. Novoselov, *Phys. Rev. B* **2013**, *87*, 081307.
[48] C. Yang, Z. Chen, I. Shakir, Y. Xu, H. Lu, *Nano Res.* **2016**, *9*, 951.
[49] P. Colomban, S. Folch, A. Gruger, *Macromolecules* **1999**, *32*, 3080.
[50] S. Xu, J. Sun, L.Weng, Y. Hua, W. Liu, A. Neville, M. Hu, X. Gao, *Appl. Surf. Sci.* **2018**, *447*, 368.
[51] N. Maity, A. Mandal, A. K. Nandi, *J. Mater. Chem.* **2017**, *5*, 12121.
[52] S. Uppugalla, P. Srinivasan, *J. Solid State Electrochem.* **2019**, *23*, 295.
[53] Y. Tian, S. Cong, W. Su, H. Chen, Q. Li, F. Geng, Z. Zhao, *Nano Lett.* **2014**, *14*, 2150.
[54] S. Kiruthika, G. U. Kulkarni, *Energy Technol.* **2020**, *8*, 1901364.
[55] Z. Jiang, Y. Wang, S. Yuan, L. Shi, N. Wang, J. Xiong, W. Lai, X. Wang, F. Kang, W. Lin, C. P. Wong, *Adv. Funct. Mater.* **2019**, *29*, 1807116.
[56] B. Hu, X. Qin, A. M. Asiri, K. A. Alamry, A. O. Al-Youbi, X. Sun, *Electrochem. Commun.* **2013**, *28*, 75.
[57] K. Sheng, Y. Sun, C. Li, W. Yuan, G. Shi, *Sci. Rep.* **2012**, *2*, 247.
[58] S. Hussain, I. Rabani , D. Vikraman, A. Feroze , M. Ali, Y. S. Seo , H. S. Kim, S. H. Chun , J. Jung, *Nanomaterials* **2020**, *10*, 1597.
[59] J. Gao, Y. Ma, J. Li, J. Fan, P. Shi, Q. Xu, Y. Min, *J. Nanopart. Res.* **2018**, *20*, 298.
[60] T. Yang, L. Meng, H. Chen, S. Luo, W. Li, K. Jiao, *Adv. Mater. Interfaces* **2016**, *3*, 1500700.
[61] A. Ramadoss, T. Kim, G. S. Kim, S. J. Kim, *New J. Chem.* **2014**, *38*, 2379.
[62] M. A. Bissett, I. A. Kinloch, R. A. Dryfe, *ACS Appl. Mater. Interfaces* **2015**, *7*, 17388.
[63] S. Ardizzone, G. Fregonara, S. Trasatti, *Electrochim. Acta* **1990**, *35*, 263.
[64] I. D. Raistrick, in *The Electrochemistry of Semiconductors and Electronics–Processes and Devices* (Eds: J. McHardy, F. Ludwig), Noyes Publication, Park Ridge **1992**, p. 297.
[65] R. de Levie, *Adv. Electrochem. Electrochem. Eng.* **1967**, *6*, 329.
[66] P. Zhang, F. Wang, M. Yu, X. Zhuang, X. Feng, *Chem. Soc. Rev.* **2018**, *47*, 7426.
[67] J. Joseph, A. Paravannoor, S. V. Nair, Z. J. Han, K. K. Ostrikov, A. Balakrishnan, *J. Mater. Chem. A* **2015**, *3*, 14105.
[68] N. Islam, S. Li, G. Ren, Y. Zu, J. Warzywoda, S. Wang, Z. Fan, *Nano Energy* **2017**, *40*, 107.
[69] M. Zhao, J. Nie, H. Li, M. Xia, M. Liu, Z. Zhang, X. Liang, R. Qi, Z. L. Wang, X. Lu, *Nano Energy* **2019**, *55*, 447.
[70] D. Pech, M. Brunet, H. Durou, P. Huang, V. Mochalin, Y. Gogotsi, P.-L. L. Taberna, P. Simon, *Nat. Nanotechnol.* **2010**, *5*, 651.
[71] N. Kurra, M. K. Hota, H. N. Alshareef, *Nano Energy* **2015**, *13*, 500.
[72] B. E. Conway, *Electrochemical Supercapacitors*, 1st ed., Springer, New York **1999**.
[73] Y. Zhu, S. Murali, M. D. Stoller, K. J. Ganesh, W. Cai, P. J. Ferreira, A. Pirkle, R. M. Wallace, K. A. Cychosz, M. Thommes, D. Su, E. A. Stach, R. S. Ruoff, *Science* **2011**, *332*, 1537.
[74] S. Mondal, U. Rana, S. Malik, *J. Phys. Chem. C* **2017**, *121*, 7573.
[75] A. Viswanthan, A. N. Shetty, *AIP Conf. Proc.* **2018**, *1943*, 020066.
[76] M. D. Stoller, R. S. Ruoff, *Energy Environ. Sci.* **2010**, *3*, 1294.
[77] F. Chi, C. Li, Q. Zhou, M. Zhang, J. Chen, X. Yu, G. Shi, *Adv. Energy Mater.* **2017**, *7*, 1700591.
[78] G. Ren, S. Li, Z.-X. Fan, M. N. F. Hoque, Z. Fan, *J. Power Sources* **2016**, *325*, 152.
[79] V. Shrivastav, S. Sundriyal, P. Goel, V. Shrivastav, U. K. Tiwari, A. Deep, *Electrochim. Acta* **2020**, *345*, 136194.
[80] L. Li, J. Gao, V. Cecen, J. Fan, P. Shi, Q. Xu , Y. Min, *ACS Omega* **2020**, *5*, 4657.
[81] C. Meng, C. Liu, L. Chen, C. Hu, S. Fan, *Nano Lett.* **2010**, *10*, 4025.

